batteries

MDPI

Article

In Situ Metal Organic Framework (ZIF-8) and Mechanofusion-Assisted MWCNT Coating of $LiFePO_4$/C Composite Material for Lithium-Ion Batteries

Priyatrisha Mathur [1,2], Jeng-Ywan Shih [2], Ying-Jeng James Li [1,2], Tai-Feng Hung [1], Balamurugan Thirumalraj [3], Sayee Kannan Ramaraj [4], Rajan Jose [5], Chelladurai Karuppiah [1,*] and Chun-Chen Yang [1,2,6,*]

1 Battery Research Center of Green Energy, Ming Chi University of Technology, New Taipei City 24301, Taiwan
2 Department of Chemical Engineering, Ming Chi University of Technology, New Taipei City 24301, Taiwan
3 School of Materials Science & Engineering, Kookmin University, Seoul 02707, Republic of Korea
4 PG and Research Department of Chemistry, Thiagarajar College, Madurai 625706, India
5 Nanostructured Renewable Energy Materials Laboratory, Faculty of Industrial Sciences and Technology, Universiti Malaysia Pahang, Kuantan 26300, Malaysia
6 Department of Chemical and Materials Engineering, Chang Gung University, Kwei-shan, Taoyuan 333, Taiwan
* Correspondence: kcdurai.rmd@gmail.com (C.K.); ccyang@mail.mcut.edu.tw (C.-C.Y.); Tel.: +886-2-29089899 (ext. 4962 or 4952) (C.K.); Fax: +886-2-29085941 (C.K.)

Abstract: $LiFePO_4$ is one of the industrial, scalable cathode materials in lithium-ion battery production, due to its cost-effectiveness and environmental friendliness. However, the electrochemical performance of $LiFePO_4$ in high current rate operation is still limited, due to its poor ionic- and electron-conductive properties. In this study, a zeolitic imidazolate framework (ZIF-8) and multi-walled carbon nanotubes (MWCNT) modified $LiFePO_4$/C (LFP) composite cathode materials were developed and investigated in detail. The ZIF-8 and MWCNT can be used as ionic- and electron-conductive materials, respectively. The surface modification of LFP by ZIF-8 and MWCNT was carried out through in situ wet chemical and mechanical alloy coating. The as-synthesized materials were scrutinized via various characterization methods, such as XRD, SEM, EDX, etc., to determine the material microstructure, morphology, phase, chemical composition, etc. The uniform and stable spherical morphology of LFP composites was obtained when the ZIF-8 coating was processed by the agitator [A], instead of the magnetic stirrer [MS], condition. It was found that the (optimum of) 2 wt.% ZIF-8@LFP [A]/MWCNT composite cathode material exhibited outstanding improvement in high-rate performance; it maintained the discharge capacities of 125 mAh g^{-1} at 1C, 110 mAh g^{-1} at 3C, 103 mAh g^{-1} at 5C, and 91 mAh g^{-1} at 10C. Better cycling stability with capacity retention of 75.82% at 1C for 100 cycles, as compared to other electrodes prepared in this study, was also revealed. These excellent results were mainly obtained because of the improvement of lithium-ion transport properties, less polarization effect, and interfacial impedance of the LFP composite cathode materials derived from the synergistic effect of both ZIF-8 and MWCNT coating materials.

Keywords: surface coating; olivine type cathode materials; energy storage; MWCNT materials; metal-organic frameworks; ZIF-8

Citation: Mathur, P.; Shih, J.-Y.; Li, Y.-J.J.; Hung, T.-F.; Thirumalraj, B.; Ramaraj, S.K.; Jose, R.; Karuppiah, C.; Yang, C.-C. In Situ Metal Organic Framework (ZIF-8) and Mechanofusion-Assisted MWCNT Coating of $LiFePO_4$/C Composite Material for Lithium-Ion Batteries. *Batteries* **2023**, *9*, 182. https://doi.org/10.3390/batteries9030182

Academic Editors: Marco Giorgetti and Biao Li

Received: 31 December 2022
Revised: 3 March 2023
Accepted: 18 March 2023
Published: 20 March 2023

1. Introduction

$LiFePO_4$, a cathode material with an olivine structure, is a competitive cathode material for commercialization in lithium-ion batteries, due to its high redox potential of Fe^{2+}/Fe^{3+} (3.45 V vs. Li/Li^+), stable structure, and the theoretical capacity reaches to 170 mAh g^{-1}. Comparatively, the longer cycle life, environmentally benign nature, safety, and stability make $LiFePO_4$ a lucrative choice for the automobile industry. Although $LiFePO_4$ itself has various limitations, such as self-discharging, low lithium-ion

diffusion coefficient (*ca.* 10^{-14}–10^{-16} cm^2 s^{-1}), and low intrinsic electronic conductivity (*ca.* 10^{-9}–10^{-10} S cm^{-1}) [1–4], numerous methods, including particle size reduction, composite formation, incorporation of dopants and functionalization, altering particle morphology, suitable encapsulation of active materials, and modification of electrolytes, have been explored and studied to overcome those limitations in $LiFePO_4$ [3–7]. Specifically, surface modification strategies on $LiFePO_4$ cathode materials have played an essential role in enhancing the electrochemical performance by improving its lithium-ion diffusivity or electron conductivity [3,8–10].

Surface modification mainly plays a prominent role in preventing $LiFePO_4$ particles from directly contacting the electrolytes and reducing Fe dissolution. It is also considered a potential method not only involved in protecting the $LiFePO_4$ from the HF attack, but also enabling both electron- and ion-conducting channels to enhance the electrochemical performance [11]. A dual conductivity-based surface modification has been explored and provided a stable and better conductive interface in $LiFePO_4$-based LIBs by reducing the interfacial resistance and balancing the charge transfer properties. For instance, $Li_{1.4}Al_{0.4}Ti_{1.6}(PO_4)_3$ (LATP) and graphene nanosheets (GNS) hybrid layers can significantly improve both the ion-/electron-conducting properties of $LiFePO_4$ and deliver high discharge capacity of 130 mAh g^{-1} at a current rate of 10C [12]. The dual conductivity nature can also be achieved by fluorine-doped carbon coating on $LiFePO_4$, which can efficiently promote the ion/electron transfer and enhance the rate capability [3]. A hybrid conductive layer modification based on LATP@C to the $LiFePO_4$ performs intense activity at a high current rate of up to 60C [13]. Hence, the surface modification of $LiFePO_4$ with a dual conductive layer, is a promising strategy for improving the cathode materials' sustainability in high-rate performance.

In recent years, metal-organic frameworks (MOFs) have experienced unprecedented interest, due to their multifunctionality and versatility. Some unique structural properties, including tunable porosity, uniform pore structure, and structural uniformity at an atomic level, have been attracted and utilized in gas and liquid adsorption, gas storage, sensing, battery, and supercapacitor applications [14–19]. Zeolitic imidazolate frameworks (ZIF) fall under the subcategory of MOFs that comprise tetrahedrally coordinated transition metal ions (such as cobalt, copper, iron, and zinc) bridged by imidazolates [20]. Many potential applications for various ZIF materials have been envisioned, since it displays tunable porosity, high surface area, multiple functionalities, and thermal and chemical stability [21]. Zeolitic imidazolate framework-8 (ZIF-8) consists of metallic zinc and ligands forming 2-methylimidazole coordinated in a framework structure. The metal-imidazole-metal angle exhibits structural similarity to the 145° Si-O-Si angle and, thus, makes them isomorphic [22]. Many ZIF topologies have been discovered; undoubtedly, more are coming. As a result of the vigorous porosity, thermal resistance, and stability of chemical reactions, ZIFs are considered for a vast array of applications. Li et al. developed a ZIF-8-modified $LiNi_{1/3}Co_{1/3}Mn_{1/3}O_2$ (NCM333) cathode material for lithium-ion battery application [23]. The deposition of ZIF-8 occurs only on the surface and is not embedded into the host lattice. The results demonstrate that the ZIF-8-modified NCM333 exhibits high discharge capacity and retention relative to the unmodified NCM333 for 200 cycles. Xu et al. synthesized mesoporous carbon derived from ZIF-8, which can improve both the ion-/electron-conductive properties of $LiFePO_4$ and high rate cycling performances with the retention of 99.9% after 60 cycles at 10C rate [24]. Xu et al. also prepared a $LiFePO_4$ composite cathode based on the surface modification of a metallic-zinc-containing graphitic carbon coating layer (about 10 nm) that was derived from the pyrolysis of ZIF-8 material [25]. The $LiFePO_4@C_{ZIF\text{-}8}$ cathode displayed a high discharge specific energy of 141.7 mAh g^{-1} after the completion of 200 cycles at 5C with 99% capacity retention. The above results reveal that the existence of micro/mesoporosity in ZIF-8 and its derived carbon materials facilitates high electrolyte permeability and Li^+ ion diffusivity by shortening the path length of mass and charge transport, thus enhancing the electrochemical performances.

The state-of-the-art explores that incorporating multiple conductive carbon modification strategies on the cathode materials has exhibited higher rate capability and better electrochemical cycling stability at room temperature [10,26–28]. The conductive carbon adopts the role of a complex wiring channel that interconnects the $LiFePO_4$ particles—implementing carbon nanotubes (CNTs) and GNS as carbon source permits the entire $LiFePO_4$ electrode to be composed of a conductive 3D network [29–31]. Adversely, the electrical conductivity may be poor, due to the absence of proper contact of the individual $LiFePO_4$ particle surface with the carbon source. Moreover, the arbitrary incorporation of CNTs, due to their poor dispersibility in solution, may lead to inefficient utilization of its conductive network. Therefore, the cathode materials have been mixed externally by a dry-coating process, which includes hand mixing in mortar, solid-state ball milling, and mechanical alloy coating strategies [5,32,33]. Sharmila et al. prepared $LiMnPO_4$@MWCNT material by the simple solid-state method via grinding by mortar and pestle [34]. The porosity and interconnecting channels of nanotubes promoted ion diffusion and improved the electrode/electrolyte interface, thus providing better electrochemical results. Our recent reports demonstrated that the dry-coating of LATP contained porous carbon additives (dual conductive coating layer) on high voltage cathode materials, i.e., Ni-rich $LiNi_{0.8}Co_{0.1}Mn_{0.1}O_2$ (4.3 V vs. Li/Li^+) and $LiFe_{1/3}Mn_{1/3}Co_{1/3}PO_4/C$ (5.0 V vs. Li/Li^+) by a mechanical alloy method [32,35]. Both the cathodes exhibited a better rate capability and cyclability at a high current rate, due to their improved ionic conductivity and interfacial resistance.

In this work, we demonstrate a dual conductive (ion/electron) surface modification strategy based on ZIF-8 coating by an in situ solution process and multiwalled carbon nanotube (MWCNT) coating by a mechanical alloy dry-coating method to develop a $LiFePO_4/C$ (LFP/C) composite cathode material. Here, the in situ ZIF-8 coating can efficiently regulate the Li^+ ion transport to the LFP particles. At the same time, the MWCNT fillers can help cause more uniform electron conduction throughout the adjacent secondary LFP particles. A magnetic stirring method initially optimized the amount (1, 2, 3, and 4 wt.%) of ZIF-8 coating. Further, we have compared the optimum ZIF-8 (2 wt.%) coating based on the magnetic stirring method with the agitating method. On the other hand, adding MWCNT in the mechanical alloy process is more beneficial for increasing the electron conductivity properties of the 2 wt.% ZIF-8@LFP cathode materials, due to the highly conductive one-dimensional nanostructure of MWCNT. Galvanostatic charge/discharge tests were implemented at various C–rates within the voltage range of 2.0–3.8 V (vs Li/Li^+). Our results found that the integration of conductive carbon filler (2 wt.% MWCNT) and the 2 wt.% ZIF-8 on LFP significantly increased the electron and lithium-ion conductivity, thus improving the high rate discharge capacity of 103 mAh g^{-1} (5C) and 91 mAh g^{-1} (10C), which is far better than the previous report regarding LFP coated with micro/mesoporous carbon derived from ZIF-8. The Coulombic efficiency and capacity retention also benefit from this modification. Hence, the modification of commercial LFP with an in situ coating of 2 wt.% ZIF-8 and 2 wt.% MWCNT makes it a suitable approach for new LFP cathode materials in lithium-ion batteries.

2. Experimental Section

2.1. Preparation of ZIF-8

Zinc nitrate hexahydrate (Sigma-Aldrich chemicals, Taipei, Taiwan) and 2-methylimida zole (2-MeIm; Sigma-Aldrich chemicals, Taipei, Taiwan) were mixed in ethanol at the molar ratio of 1:8. The resultant mixture was stirred continuously for 24 h using a magnetic stirrer to form the ZIF-8 particles. After centrifugation at 9000 rpm for 15 min, the supernatant was discarded, and the white pellet left at the bottom was collected and dried overnight at 80 °C to obtain the ZIF-8 particles. Morphology studies confirmed the formation of the preferred ZIF-8 particles. Additionally, it must be noted that the yield percentage of the resultant ZIF-8 was only roughly 25% of the total amount of zinc nitrate hexahydrate used

initially. This result is crucial to guarantee the different weight compositions of the ZIF-8 deposited on LFP, in order to determine the optimal ZIF-8 content.

2.2. Preparation of ZIF-8-Modified LFP Composite by a Magnetic Stirrer Method

Commercially available $LiFePO_4/C$ cathode material (5005 product, Formosa Materials, Taipei, Taiwan) was modified by surface-deposition of ZIF-8 dodecahedron nanoparticles. In brief, 5 g of commercial LFP powder was added into 70 mL ethanol-containing beaker; then, the mixture was ultrasonicated for 30 min to obtain a uniform dispersion by the ultrasonic cleaner DC300Hz (Delta Ultrasonic Co. Ltd., New Taipei City, Taiwan). Following this, the synthesis of the ZIF-8 particles was carried out using the molar ratio of 1:8 (Zinc nitrate hexahydrate: 2-MeIm), as mentioned above, under the magnetic stirring condition at about 350 rpm. A suspension of ethanolic 2-MeIm (7.03 mmol) was slowly added to the LFP/ethanol solution by a peristaltic pump setup with the constant stirring condition for 24 h. Then, ethanolic zinc nitrate hexahydrate (~0.88 mmol) solution was added using the same technique mentioned above and kept constant stirring for 24 h. The residue was collected after centrifugation and washed with ethanol three times. Finally, the ZIF-8@LFP composite was received after drying at 80 °C in a hot air oven. The different ZIF-8@LFP samples were prepared in this work by varying the deposition amount of ZIF-8 by 1, 2, 3, and 4 wt.%, named as 1 wt.% of ZIF-8, 2 wt.% of ZIF-8, 4 wt.% of ZIF-8, and 4 wt.% of ZIF-8, respectively. A detailed information about various amount of ZIF-8 coating can be found in the Supporting Information, see Table S1.

2.3. Preparation of 2 wt.% ZIF-8@LFP Composite by an Agitator Method

The optimum of 2 wt.% ZIF-8@LFP composite cathode material was also prepared by an agitator (DC Motor; New Lab Instruments Co. Ltd., New Taipei City, Taiwan) technique. A four-blade paddle was used as the agitator, rotated at a speed of about 450 rpm. A total of 5 g LFP in 70 mL ethanol was treated by ultrasonication for 30 min and followed by 24 h agitation to form a uniform suspension. The surface coating of 2 wt.% ZIF-8 on LFP was carried out under similar conditions mentioned in Section 2.2. Finally, the obtained composite product was referred to as 2 wt.% ZIF-8@LFP [A].

2.4. Preparation of 2 wt.% ZIF-8@LFP/MWCNT Composite by a Dry-Coating Method

After the preparation of 2 wt.%ZIF-8@LFP [A], based on the experimental condition mentioned in the Sections 2.2 and 2.3, the dry-coating was performed using 2 wt.% MWCNT in mechanofusion apparatus (Hosokawa micron corporation, Tokyo, Japan). The mechanofusion milling was conducted at the rotation speed of 4500 rpm for 1 min, with five intervals [35].

2.5. Instrumentation

Scanning electron microscopy (SEM) was used to analyze the surface morphology of the synthesized materials by JSM-IT200 (JEOL Inc, Pleasanton, CA, USA). Elemental analysis was also carried out with Oxford Xplore 30 EDS (Oxford Instruments, Beaverton, OR, USA). Phase purity of the materials was studied by X-ray diffraction (XRD) analyzer (BRUKER D2 PHASER, Karlsruhe, Germany) at 40 kV and 50 mA, with Cu-Kα (λ = 0.1534 nm). Micro-Raman spectroscopy (Confocal micro Renishaw, Gloucestershire, UK) with 632 nm He–Ne was also performed. Charge/discharge tester (Arbin BT-2043, 0.1 A, Charger, ALT Inc, East Lyme, CT, USA). Electrochemical analysis workstation PG-STAT302N (Metrohm Autolab B. V., Houten, The Netherlands).

2.6. Electrode Fabrication and Measurements

The commercial LFP or as-modified composite LFP powders were used as the active material. The slurry composition is maintained with the ratio of 8:1:1 (wt.%) by the active material: polyvinylidene fluoride (PVDF): Super P, respectively. In slurry preparation, 2 g of the active material is sieved with the help of a sieving mesh (0.044 μm). The fine

powder, thus, obtained is incorporated with a suitable amount of Super P by a mortar and pestle. The powders are then baked in a 120 °C oven for 1 h to remove any traces of moisture. A mixture of PVDF and N-methyl-2-pyrrolidone (NMP) is combined in a stirrer and stirred at 150 rpm for 30 min. Active material and Super P are slowly added along with additional suitable amounts of NMP (if required). The mixture is stirred at 450 rpm for 3 h, with a subsequent stirring for 1 h at 110 rpm. After mixing, the slurry is coated on a current aluminum collector smoothly attached to a clean glass plate. The universal applicator is used at a wet film thickness of 200 µm for this. The glass plate with the coated slurry is placed in a 60 °C oven overnight to remove any redundant organic solvent (NMP). The as-prepared electrode was roll-pressed and cut into a circular disc with a diameter of 13 mm, and then used as the cathode to assemble the CR2032 coin cell. The active material loading achieved was approximately 2–3 mg cm^{-2}. The 2032-type coin cell fabricated using the as-prepared LFP electrode as the cathode, and pure lithium metal disc (diameter 1.6 cm; thickness 450 µm) was used as the anode, while a polyethylene membrane (PE; thickness 16 µm; Asahi Kasei, Tokyo, Japan) acted as the separator. The electrolyte used was a 1 M solution of $LiPF_6$ in ethylene carbonate (EC)/diethyl carbonate (DEC) (1:1, *v*/*v*). The actual fabrication of all the parts mentioned above took place inside a glove box (MBraun LABstar, Garching, Germany) with an argon atmosphere, which had the operating conditions of H_2O < 0.5 ppm; O_2 < 0.5 ppm. After the coin cells were assembled, they were stored idle for around 24 h to ensure the electrolyte was imbibed well into the electrode. Electrochemical impedance spectroscopy (EIS) measurement was observed in an electrochemical data testing setup (PGSTAT302N; Metrohm Autolab B. V., Utrecht, The Netherlands) at a frequency spanning 1 MHz to 0.01 Hz and at an amplitude of 0.01 VRMS.

3. Results and Discussion

3.1. Material Characterization

Preliminary experiments were conducted to prepare nano-sized ZIF-8 particles. Figure S1A,B displays SEM and XRD results to confirm the formation of ZIF-8, indicating the uniform dodecahedron nanoparticles (*ca.* 300 nm) with a high crystalline phase. The characteristic XRD peaks of ZIF-8, as shown in Figure S1B, for the planes (002), (112), (022), (013), (222), (114), (233), (134), and (044), were observed at 2θ of 10.79°, 13.12°, 15.14°,16.91°, 18.49°, 22.56°, 24.94°, 27.13°, and 30.02°, which is in good agreement with the previous literature [36]. The XRD patterns of LFP-coated ZIF-8 samples are also shown in Figure S2. To determine the optimal percentage composition of ZIF-8 on LFP, various amounts of 1, 2, 3, and 4 wt.% for ZIF-8 coating were conducted. The XRD patterns of Figure S2 curves (a)–(d) show a clear increment in the characteristic peak of (112) plane of pristine ZIF-8 upon increasing the coating amount of ZIF-8 from 1 wt.% to 4 wt.%. This signifies the successful synthesis of ZIF-8 on the LFP materials. In addition, the SEM images of Figure 1A,B show the morphology of the bare LFP and 2 wt.% ZIF-8-modified LFP microsphere powders, respectively. The results revealed that the in situ growth method could form a uniform deposition of ZIF-8 nanoparticles on the LFP microsphere powders. However, it forms agglomerated ZIF-8 particles on the LFP surface, instead of uniform distribution, when increasing the content to 3 wt.% and 4 wt.%. This can possibly increase the path length of Li^+ ion transport to the LFP lattice, which may affect the discharge capacity. Therefore, the results suggest that the 2 wt.% ZIF-8 coating is the optimum for improving the electrochemical performance.

Figure 1C,D also shows the SEM images of the 2 wt.% ZIF-8@LFP [A] samples prepared through an agitator. This method was preferred, in order to maintain the LFP microsphere morphology without any damage. The 2 wt.% ZIF-8@LFP [MS] samples prepared via a magnetic stirring method delivered severely broken particles distributed on their LFP composite mixture, which is clearly depicted in Figure 1B and Figure S3A–D. However, the 2 wt.% ZIF-8@LFP [A] samples show more uniform microsphere morphology, similar to the bare LFP. Furthermore, the LFP composite samples were further dry-coated with MWCNTs

via mechanofusion treatment. Figure 1E,F reveals the incorporation of MWCNT additives on the 2 wt.% ZIF-8@LFP [A] samples. It is further confirmed with the TEM analysis. Figure S3A,B shows the clear surface of LFP with the coating of amorphous carbon layer; however, Figure S3C,D shows the attachment of ZIF-8 and MWCNT to the carbon layer-coated LFP surface. Hence, the above morphological study indicating that the successful modification of ZIF-8 and MWCNT on the LFP materials.

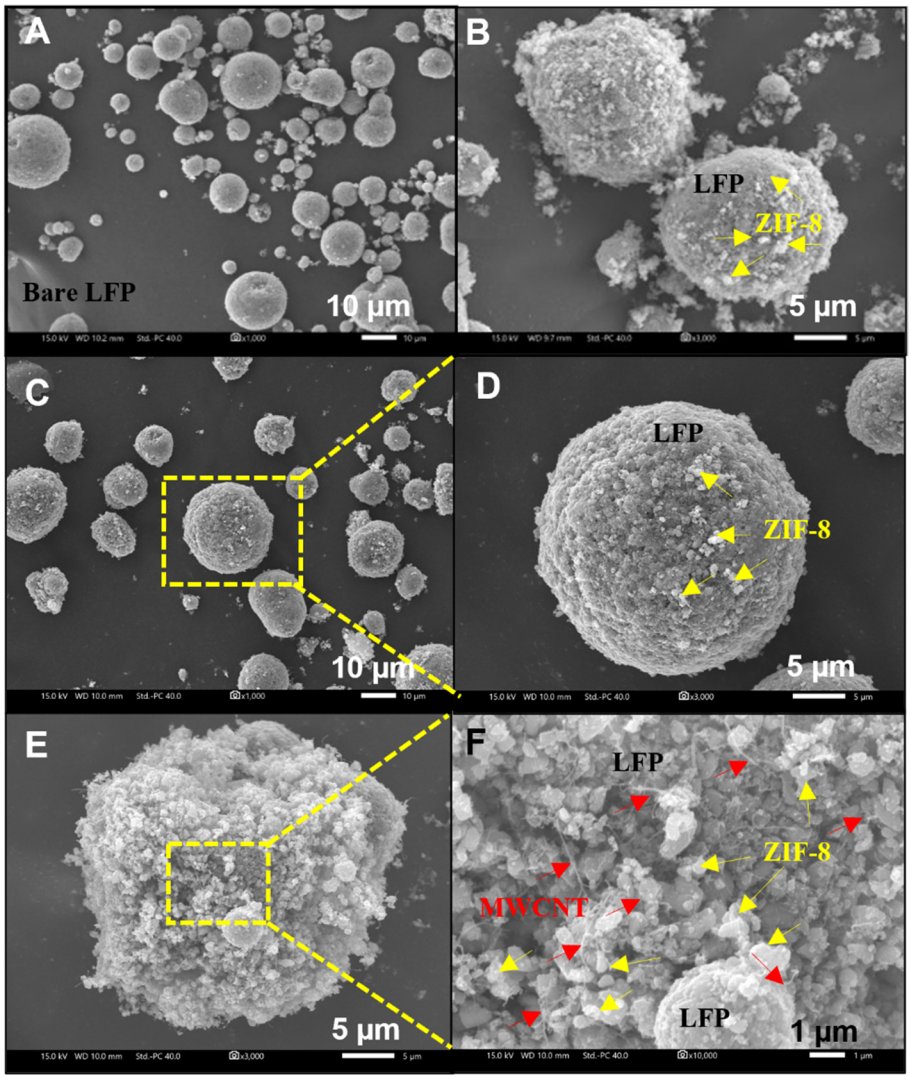

Figure 1. SEM images of the (**A**) bare LFP, (**B**) 2 wt.% ZIF-8@LFP [MS], (**C**,**D**) 2 wt.% ZIF-8@LFP [A], and (**E**,**F**) 2 wt.% ZIF-8@LFP [A]/MWCNT samples.

Figure 2 shows the EDX analysis to evaluate the element distribution in 2 wt.% ZIF-8@LFP [A]/MWCNT composite material. Figure 2A represents the EDX spectra of the 2 wt.% ZIF-8@LFP [A]/MWCNT sample, and its corresponding elemental mapping results can be seen in Figure 2B. The EDX mapping result of the elements, including iron (Fe), phosphorus (P), oxygen (O), zinc (Zn), nitrogen (N), and carbon (C), was shown in Figure 2C–H, respectively. The deposition of ZIF-8 on the LFP composite was confirmed by the presence of the zinc and nitrogen elements with significant amount. Similarly, LFP was dry-coated with the MWCNT fillers, and the number of carbons increased. Therefore, the intention of preparing an active material with a sufficient conductive carbon content to achieve better electrical conductivity has been fulfilled. Thus, an overall electrochemical performance improvement can be expected.

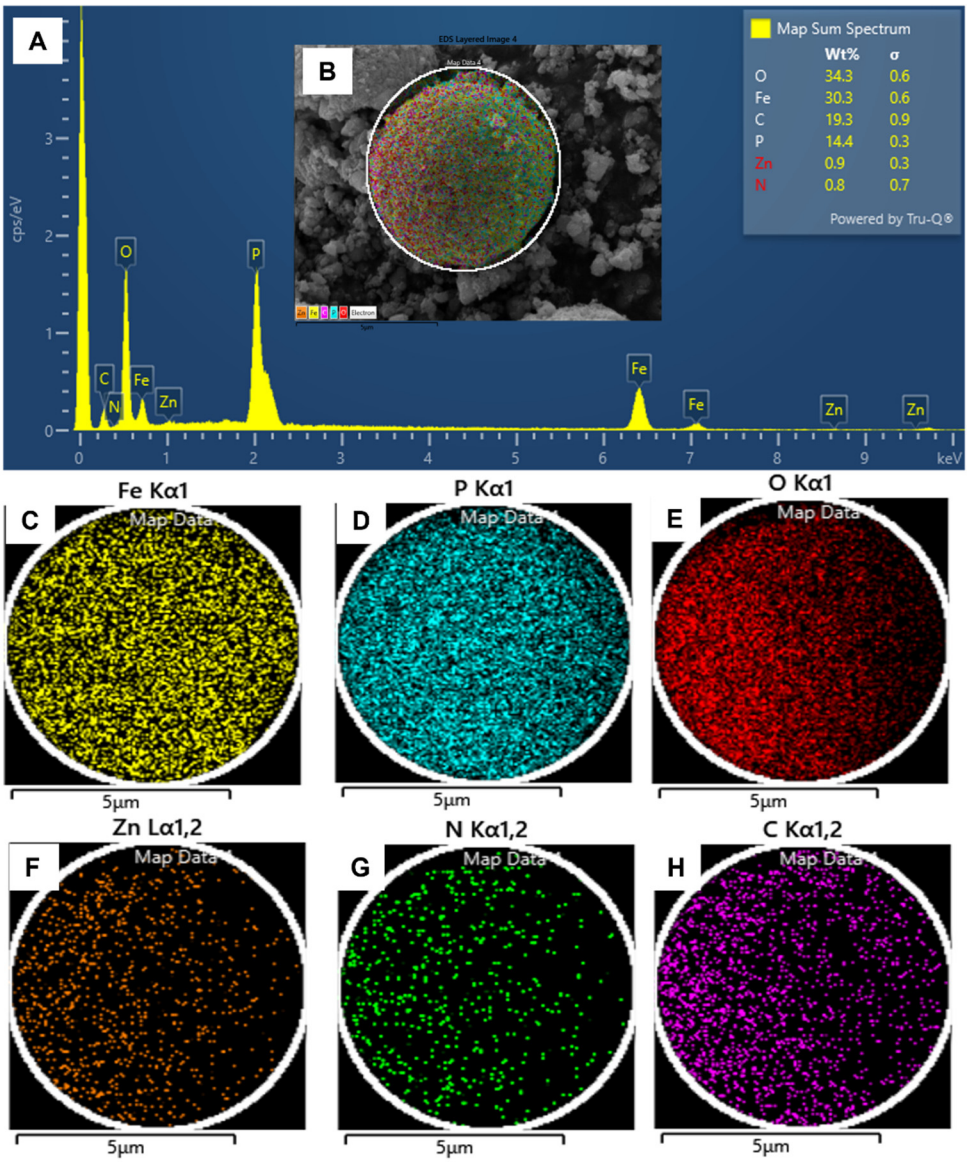

Figure 2. (**A**) EDX spectral analysis of the 2 wt.% ZIF-8@LFP [A]/MWCNT composite. (**B**) EDX mapping results of the 2 wt.% ZIF-8@LFP [A]/MWCNT sample and its corresponding elements of (**C**) iron, (**D**) phosphorus, (**E**) oxygen, (**F**) zinc, (**G**) nitrogen, and (**H**) carbon.

Figure 3A shows the comparison of XRD patterns of the pure ZIF-8 (a), bare LFP (b), 2 wt.% ZIF-8@LFP [A] (c), and 2 wt.% ZIF-8@LFP [A]/MWCNT (d) samples. Figure 3A curve (a) displays the typical crystal planes of ZIF-8, which are mentioned above. The prominent peak of the pure ZIF-8 (112) plane is exhibited on the XRD pattern of 2 wt.% ZIF-8@LFP [A] (c), which is not observed in the bare LFP sample (b). The intensity of LFP crystal planes is significantly reduced after ZIF-8 deposition, resulting from the surface modification of LFP with ZIF-8. Although, the intensity of LFP crystal planes is further decreased after dry-coating 2 wt.% of MWCNT on 2 wt.% ZIF-8@LFP [A], which is clearly seen at the peak position range of 40°–65°. Additionally, the major peak position of LFP was slightly shifted to a higher angle, about 0.2°. In comparison of the above LFP samples, it can also be observed that most of the characteristic peaks of LFP remain the same. Still, the characteristic peak (112) plane of pure ZIF-8 loses its prominence, which the presence of MWCNT may cause.

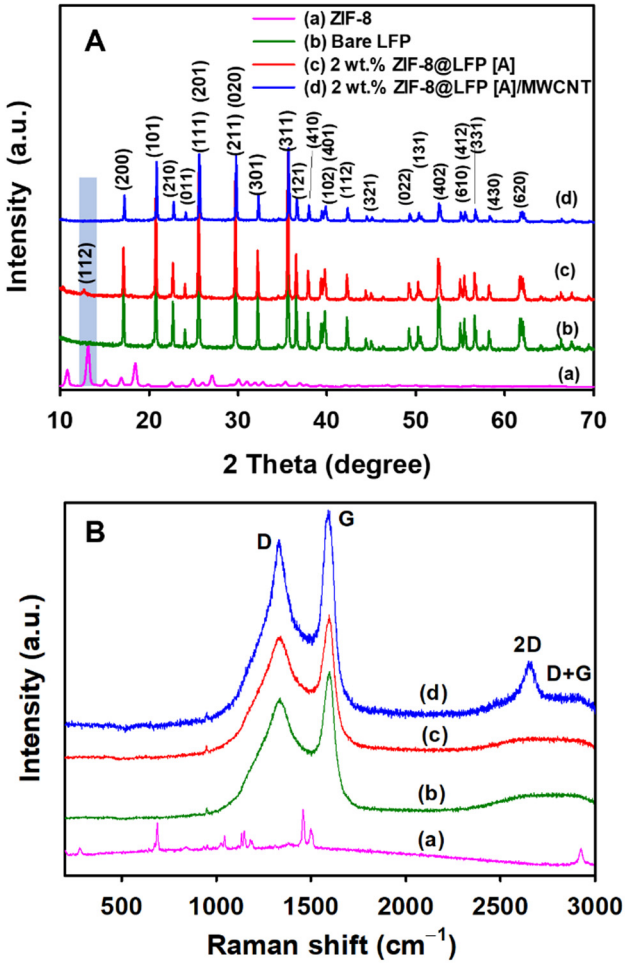

Figure 3. (**A**) XRD patterns of the pure ZIF-8 (a), bare LFP (b), 2 wt.% ZIF-8@LFP [A] (c), and 2 wt.% ZIF-8@LFP [A]/MWCNT (d) samples. (**B**) Micro-Raman spectra of the pure ZIF-8 (a), bare LFP (b), 2 wt.% ZIF-8@LFP [A] (c), and 2 wt.% ZIF-8@LFP [A]/MWCNT (d) samples.

Figure 3B depicts the micro-Raman spectroscopy of pure ZIF-8 (a), bare LFP (b), 2 wt.% ZIF-8@LFP [A] (c), and 2 wt.% ZIF-8@LFP [A]/MWCNT (d). As seen in the spectra, two strong peaks are observed for each spectrum (except pure ZIF-8) at the position of approximately 1340 and 1595 cm^{-1}, which can be assigned to the D-band (disorder band) and the G-band (graphitic band), respectively [37]. Second-order weak bands were also observed at around 2665 and 2897 cm^{-1}, ascribed to the 2D and D+G bands, respectively, which confirms the presence of highly ordered degree of carbon material [38]. The characteristic peak of PO_4^{3-} at around 950 cm^{-1} appears slightly, due to the screening effect of the MWCNTs. The peak intensity ratio of D-band and G-band (I_D/I_G) exhibits an inversely proportional relationship to the degree of graphitization of carbon [39]. The results are summarized in Table S2. The reduction in the (I_D/I_G) ratio suggests that the amount of the disordered carbon (sp^3 carbon) is lower than that of graphitic carbon (sp^2 carbon), thus increasing the graphitization degree. Additionally, the high degree of graphitization indicates higher electronic conductivity of carbon; thus, better electrochemical properties can be achieved.

XPS analyses were performed to confirm the surface elements chemical binding of the LFP composite (2 wt.% ZIF-8@LFP [A]/MWCNT) cathode materials. Figure 4 displays the elemental survey spectrum and deconvolution spectra of their corresponding elements. As seen in Figure 4A, the LFP composite cathode shows the elements of Li, P, C, N, O, Fe, and Zn, whereas the bare LFP contains only the elements of Li, P, C, O, and Fe. The peak intensities of the C 1 s (~285 eV) and O 1s (~531 eV) peaks in the LFP composite

increased and decreased, respectively, compared to the bare LFP. This phenomenon is clearly observed in the deconvolution spectra of the C 1 s (Figure 4B), O 1s (Figure S5A,B). The peak intensities were also decreased in the peaks of Fe 2p (Figure S5C,D), P 2p (Figure S5E,F), and Li 1s (Figure S5G,H). It is revealed that the surface of LFP particles shows significant modification.

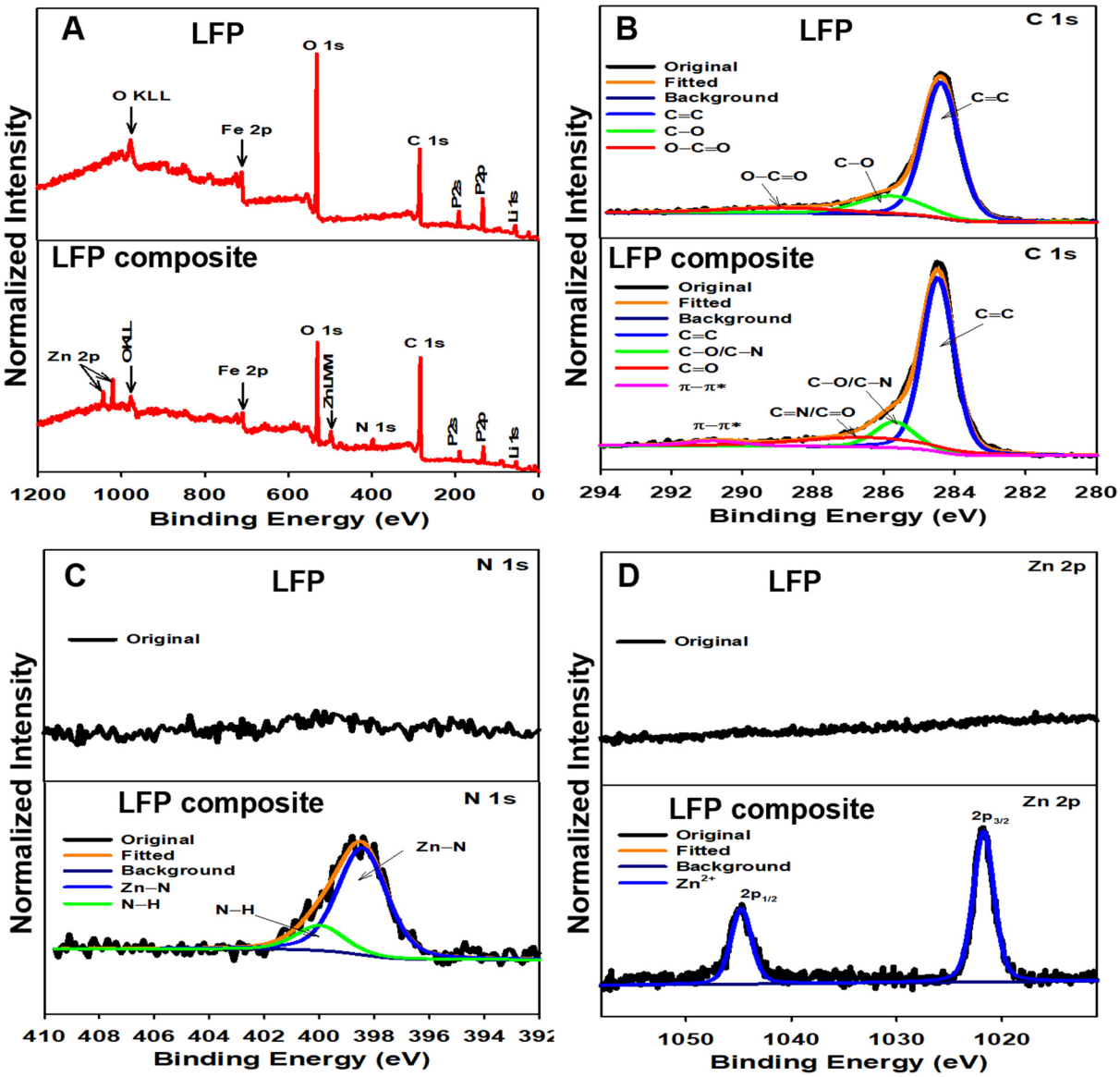

Figure 4. (**A**) Full survey spectra of the bare LFP and LFP composite (2% ZIF-8@LFP [A]/MWCNT). The deconvolution spectra of (**B**) C 1s, (**C**) N 1s, and (**D**) Zn 2p peaks of the bare LFP and LFP composite (2% ZIF-8@LFP [A]/MWCNT).

In addition, the C 1s peak of LFP composite shows the high intensity C=C peak at 284.5 eV, with some minor peaks at 285.7, 286.6, and 290.8 eV, attributed to the binding of C-O/C-N, C=O/C=N, and *p-p* *, respectively [40,41]. The appearance of the *p-p* * peak reveals the presence of highly ordered graphitic carbon in the composite samples. Additionally, the N 1s and Zn 2p peaks were only exhibited in the LFP composite, not in the bare LFP (Figure 4C). The N 1s peak of LFP composite shows two peaks at 398.5 and 400.1 eV for the Zn-N/C=N and N-H bonds in ZIF-8, respectively [42,43]. The Zn LMM peak at 497.9 eV also revealed the Zn-N bond formation [44]. The deconvolution of Zn 2p (Figure 4D) displays the spin-orbit-splitting of $2p_{3/2}$ and $2p_{1/2}$ at the binding energies

of 1021.7 and 1044.9 eV, which reveals the existence of Zn element with +2 oxidation state [42,45]. Hence, the above results confirm the surface modification of LFP by MWCNT and ZIF-8.

3.2. Electrochemical Performance

The electrochemical performance of the bare LFP and modified LFP composites was investigated using CR2023 coin-type cells under the potential range of 2.0–3.8 V (Li/Li^+). Commercial LFP was treated with different weight percentages (1, 2, 3, and 4 wt.%) of ZIF-8 nanoparticles by using the magnetic stirrer method to obtain the desired enhancement of the modified LFP cathode material. The optimal weight percentage of ZIF-8 deposited LFP was determined after electrochemical tests. Galvanostatic charge/discharge tests were performed at a charge/discharge current rate of 0.1C/0.1C, based on the bare LFP, 1 wt.% ZIF-8@LFP [MS], 2 wt.% ZIF-8@LFP [MS], 3 wt.% ZIF-8@LFP [MS], and 4 wt.% ZIF-8@LFP [MS] electrodes, corresponding to the initial cycle results, which are shown in Figure S6 curves (a)–(e), and all collected data are summarized in Table S3. The observed results indicate that the discharge capacity of the 2 wt.% ZIF-8@LFP [MS] electrode (146 mAh g^{-1}) is higher than those of the bare LFP (143 mAh g^{-1}), 1 wt.% ZIF-8@LFP [MS] (145 mAh g^{-1}), 3 wt.% ZIF-8@LFP [MS] (142 mAh g^{-1}), and 4 wt.% ZIF-8@LFP [MS] electrodes (136 mAh g^{-1}). From Table S3, our ZIF-8-modified LFP electrodes exhibit higher Coulombic efficiency (CE%) than the bare LFP electrode, which confirms the impact of the ZIF-8 coating. It significantly improved the discharge capacities and the CE% values. On the contrary, the discharge capacities decrease, while increasing the deposition amount of ZIF-8 over 2 wt.%. It may be mainly due to the aggregation of ZIF-8 particles, which may hinder the Li^+ ion transport to the LFP cathode materials. Therefore, we have chosen the 2 wt.% ZIF-8 formulation for LFP modification in further experiments.

Figure 5A further shows the comparison data of the initial charge–discharge cycle of the bare LFP (a), 2 wt.% ZIF-8@LFP [MS], 2 wt.% ZIF-8@LFP [A], and 2 wt.% ZIF-8@LFP [A]/MWCNT electrodes at 0.1C rate. All the samples exhibit a horizontal voltage plateau at 3.50 and 3.45 V during the charge–discharge process, indicating the extraction and insertion of Li^+ ions between $FePO_4$ and $LiFePO_4$. As seen in Figure 5A, the discharge capacity of the 2 wt.% ZIF-8@LFP [A] (149 mAh g^{-1}) electrode exhibits much higher results than those of the bare LFP (143 mAh g^{-1}) and 2 wt.% ZIF-8@LFP [MS] electrodes (146 mAh g^{-1}). This is due to the more compact and stable microstructure of LFP microsphere composite with the ion-conductive ZIF-8 coating, as compared to the loose microstructure particles in 2 wt.% ZIF-8@LFP [MS]. However, the discharge capacity of the 2 wt.% ZIF-8@LFP [A]/MWCNT electrode (142 mAh g^{-1}) is slightly lower than that of the other electrodes. On the contrary, the voltage polarizations at the charge–discharge plateaus were significantly reduced at the 2 wt.% ZIF-8@LFP [A]/MWCNT electrodes, which is due to the incorporation of highly electron-conductive MWCNT additives via the fast and energy-saving dry-coating process after in situ growth of ZIF-8 on LFP. As you can see in Figure 5B (the enlarged view of Figure 5A between the specific discharge capacity range of 20–80 mAh g^{-1}), the overpotential of the polarization window increased in the order of 72 mV < 96 mV < 136 mV for the bare LFP < 2 wt.% ZIF-8@LFP [MS] < 2 wt.% ZIF-8@LFP [A] electrodes. The overpotential was increased, while introducing the ZIF-8 coating. This is mainly due to the poor electron-conductive nature of the ZIF-8 materials. On the other hand, it can facilitate more Li^+ ion transport to increase the discharge capacity. This dry-coating of MWCNT can solve the limitation of electron-conductive properties of ZIF-8-modified LFP. The overpotential of 2 wt.% ZIF-8@LFP [A]/MWCNT electrode (61 mV) shows less value, as compared to the bare LFP, 2 wt.% ZIF-8@LFP [MS], and 2 wt.% ZIF-8@LFP [A] electrodes. The lesser polarization behavior is mainly due to the incorporation of MWCNT, thus improving the electron transfer kinetics of the 2 wt.% ZIF-8@LFP [A]/MWCNT composite cathode [31,46,47]. It is more beneficial to enhance the LFP cathode materials' rate capability in lithium-ion batteries.

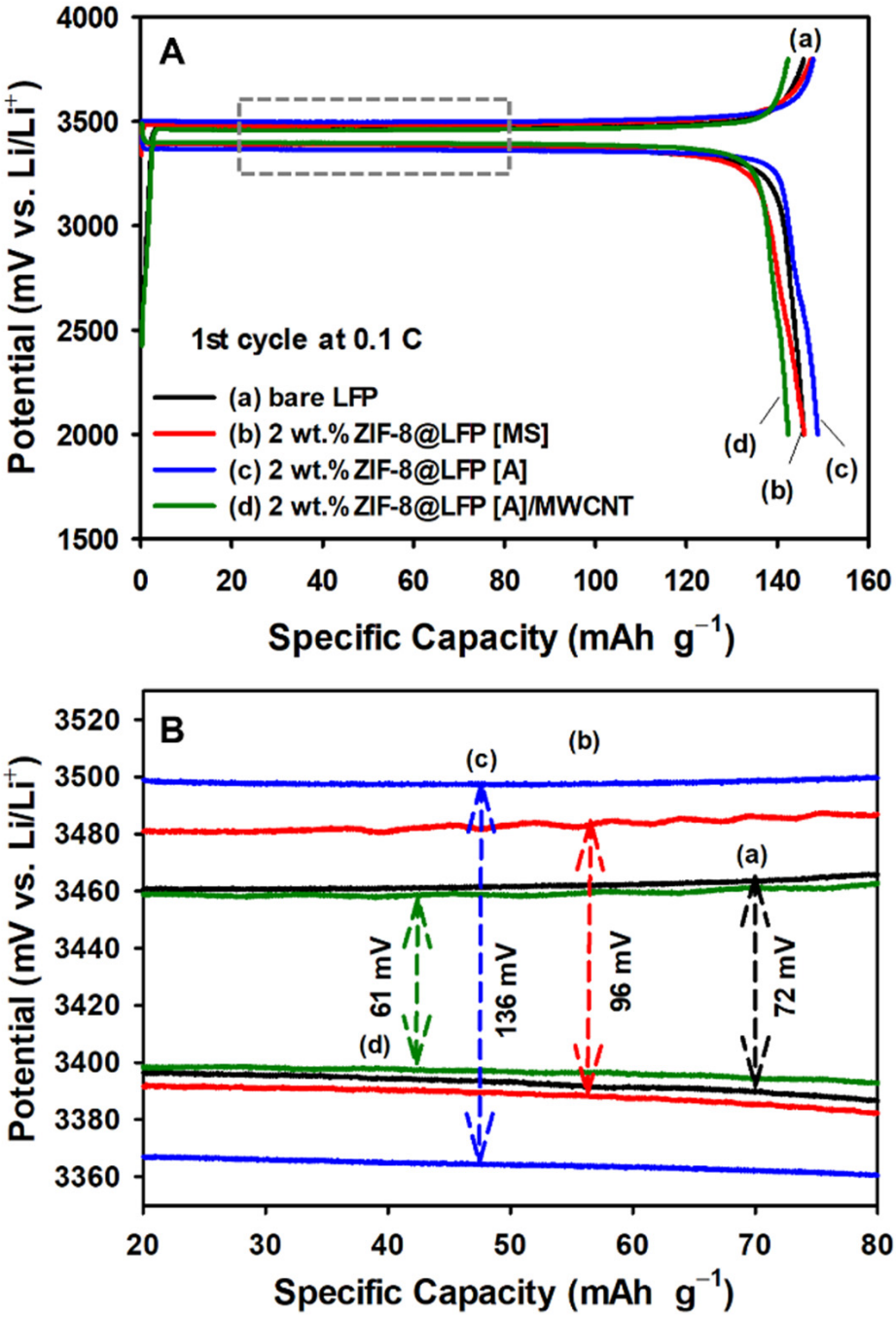

Figure 5. (**A**) First charge–discharge cycles of the bare LFP (a), 2 wt.% ZIF-8@LFP [MS], 2 wt.% ZIF-8@LFP [A], and 2 wt.% ZIF-8@LFP [A]/MWCNT electrodes at 0.1C/0.1C. (**B**) The estimation of voltage polarization from the magnified view at the selected area of Figure 4A.

The long-term cycling stability tests of the as-prepared LFP electrodes were conducted at the voltage range of 2.0–3.8 V at two different current rates, such as 0.1C/0.1C for 30 cycles and 1C/1C for 100 cycles. Figure 6A shows the cycling profile for the (a) bare LFP, (b) 2 wt.% ZIF-8@LFP [MS], (c) 2 wt.% ZIF-8@LFP [A], and (d) 2 wt.% ZIF-8@LFP [A]/MWCNT electrodes, which performed at 0.1C rate for 30 cycles, and their corresponding charge–discharge cycles are shown in Figure S7A–D. It was seen clearly that the capacity retention of the as-prepared LFP electrodes, such as the bare LFP, 2 wt.% ZIF-8@LFP [MS], 2 wt.% ZIF-8@LFP [A], and 2 wt.% ZIF-8@LFP [A]/MWCNT electrodes, had gradually improved to 88.31%, 89.34%, 90.90%, and 92.92%; the CE% were about 98.28%, 98.52%, 99.44%, and 99.58%, respectively. Furthermore, the long-term cyclability of those LFP electrodes

at 1C/1C rate is also displayed in Figure 6B. Stable charge–discharge long-term cycling and less voltage polarization behavior were observed on 2 wt.% ZIF-8@LFP [A]/MWCNT electrode (Figure 7D), as compared to bare LFP, 2 wt.% ZIF-8@LFP [MS], and 2 wt.% ZIF-8@LFP [A] electrodes (Figure 7A–C). The initial discharge capacity of 2 wt.% ZIF-8@LFP [A]/MWCNT electrode at the first cycle was around 114.65 mAh g^{-1}, which is considerably lower than that of 2 wt.% ZIF-8@LFP [A] electrode, while being close to bare LFP electrode. However, it was found that the discharge capacity did not degrade much after 100 cycles at a 1C rate. Meanwhile, the CR% and CE% values of 2 wt.% ZIF-8@LFP [A]/MWCNT electrode were significantly improved to around 75.82% and 98.95%, rather than about 65.31% and 98.08% for the bare LFP, about 69.30% and 98.40% for 2 wt.% ZIF-8@LFP [MS], and about 73.83% and 98.55% for 2 wt.% ZIF-8@LFP [A], respectively. Our results indicated that the gradual increase of CR% is due to the presence of the ZIF-8 particles on the stable structure of LFP composite materials. The stability in CE% curve of 2 wt.% ZIF-8@LFP [A]/MWCNT electrode is much more stable than those of the other LFP electrodes, where the CE curves were unstable. In addition, the voltage fading is an important factor for investigating the cyclability of the cathode materials, rather than the capacity fading [48]. Figure S8 shows the average discharge voltage and voltage efficiency profile of the (a) bare LFP, (b) 2 wt.% ZIF-8@LFP [MS], (c) 2 wt.% ZIF-8@LFP [A], and (d) 2 wt.% ZIF-8@LFP [A]/MWCNT electrodes. The voltage polarization (ΔE) effects of these above-mentioned electrodes are about 489, 542, 466, and 439 mV, respectively. The average voltage efficiencies of these electrodes are also calculated to 86.32%, 84.91%, 86.88%, and 87.59%, respectively. These results indicate that the voltage fading is clearly suppressed by the incorporation of ZIF-8 and MWCNT to the LFP cathode materials. However, the severe fading can be obtained due to the cracking or breakage of the secondary particles on the electrode surface. The specific energy density of these half-cells is calculated from the average voltage of the 100th cycle, based on the active cathode material weight, and we compared the results. The specific energy densities of the bare LFP, 2 wt.% ZIF-8@LFP [MS], 2 wt.% ZIF-8@LFP [A], and 2 wt.% ZIF-8@LFP [A]/MWCNT half-cells are about 212, 223, 238, and 242 Wh kg^{-1}, respectively. The energy efficiencies of these half-cells are about 76.77%, 77.59, 77.66%, and 78.62%, respectively. Based on the above results, it is clear that the 2 wt.% ZIF-8@LFP [A]/MWCNT delivers better performance than the other electrodes.

The post-mortem analysis of the SEM images is further verified, in that the 2 wt.% ZIF-8@LFP [A]/MWCNT electrode did not show many cracks on the surface before (Figure S9A) and after (Figure S9B) cycling at a 1C rate, compared to the bare LFP (Figure S9C,D). Additionally, the crystal structure (from XRD pattern, Figure S10A,B) and the elemental composition (from EDX analysis, Figure S11A,B) of the 2 wt.% ZIF-8@LFP [A]/MWCNT electrode did not show any significant differences after long cycles. Our results suggest that this novel strategy, based on ZIF-8 deposition and MWCNT dry-coating, offers both ionic and electronic conductivity enhancement, respectively, and facilitates the stable electrode fabrication for the LFP cathode material.

Figure 8A demonstrates the rate performance of the bare LFP (a), 2 wt.% ZIF-8@LFP [MS] (b), 2 wt.% ZIF-8@LFP [A] (c), and 2 wt.% ZIF-8@LFP [A]/MWCNT (d) electrodes at various current rates, i.e., 0.2C–10C rates, and the corresponding charge–discharge profiles can be found in Figure S12A–D. The obtained discharge capacities at 0.2C, 0.5C, 1C, 3C, 5C, and 10C for the bare LFP electrode are 127, 123, 116, 103, 93, and 74 mAh g^{-1}, respectively; for 2 wt.% ZIF-8@LFP [MS], they are 129, 125, 118, 105, 95, and 75 mAh g^{-1}, respectively; for 2 wt.% ZIF-8@LFP [A], they are 133, 126, 120, 105, 96, and 80 mAh g^{-1}, respectively; for 2 wt.% ZIF-8@LFP [A]/MWCNT, they are 137, 131, 125, 110, 103, and 91 mAh g^{-1}, respectively. Our results indicated that 2 wt.% ZIF-8 modification at LFP cathode material significantly improved the high-rate capacity, compared to the unmodified LFP cathode material. After the 10C rate, the capacity retention (CR%) for bare LFP had been estimated to be 54.78%, while maintaining an average coulombic efficiency (CE%) of 94.82%. On the contrary, the CR% of 2 wt.% ZIF-8@LFP [MS] and 2 wt.% ZIF-8@LFP [A] electrodes are approximately 57.30% and 61.23%, while maintaining CE% of 96.77% and 97.98%,

respectively. Furthermore, the 2 wt.% ZIF-8@LFP [A]/MWCNT electrode exhibits more rate capability than the other three electrodes, showing very high discharge capacities in all C-rates, especially at 5C (*ca.* 103 mAh g^{-1}) and 10C (*ca.* 91 mAh g^{-1}). It is more comparable to the high-rate capacities of 2 wt.% ZIF-8@LFP [A]/MWCNT electrodes with the previous reports (see Table 1) [13,24,25,47,49,50]. The average CE% increases to around 98.88%, and the capacity retention reaches 66.60%. It is mainly due to the synergistic effect of ZIF-8 and MWCNT dual-coating on the LFP material. Both provide highly ionic and electron-conductive environments to improve high-rate performance.

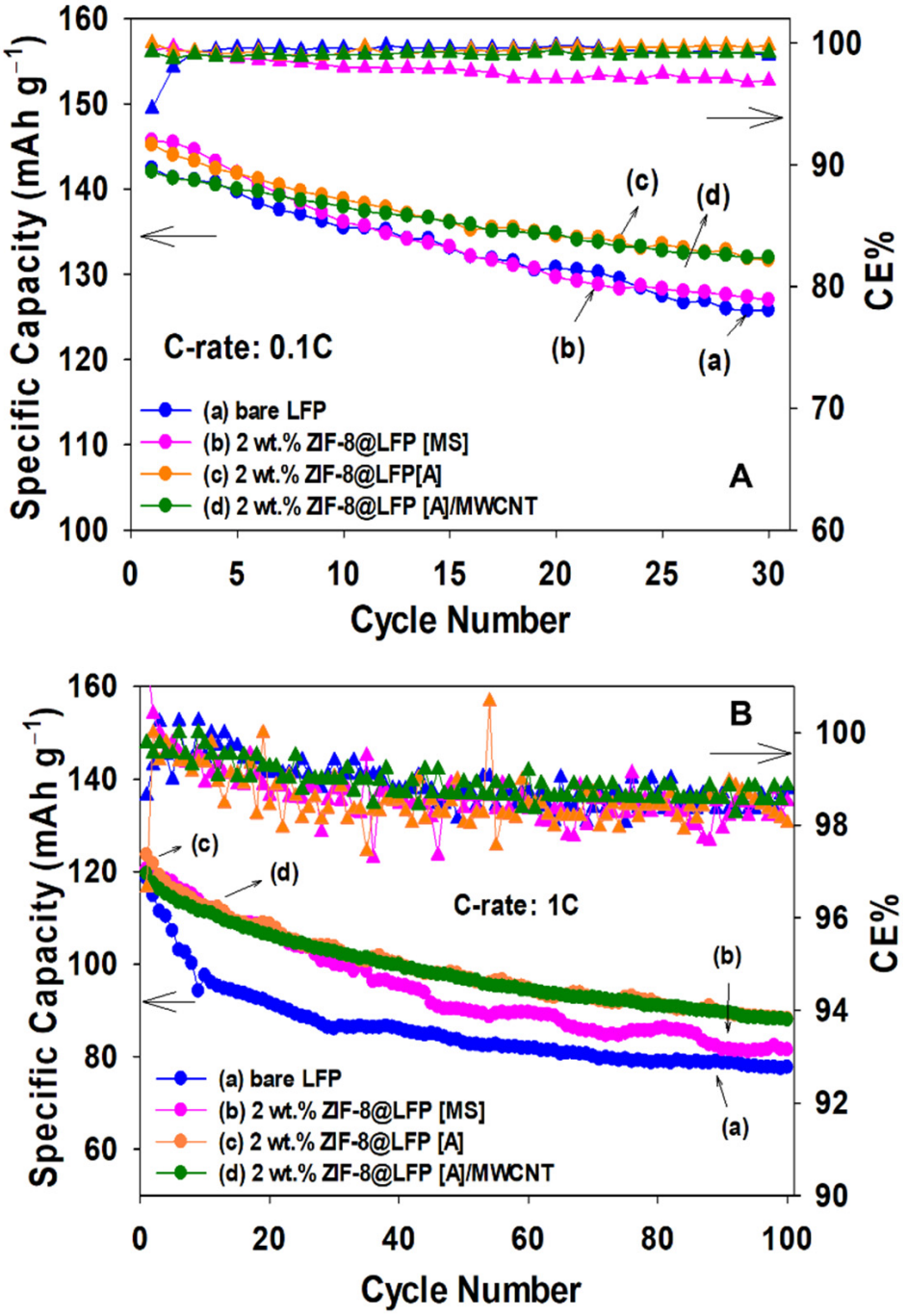

Figure 6. Cycle stability curves of the (a) bare LFP, (b) 2 wt.% ZIF-8@LFP [MS], (c) 2 wt.% ZIF-8@LFP [A] and (d) 2 wt.% ZIF-8@LFP [A]/MWCNT electrodes at 0.1C/0.1C rate for 30 cycles (**A**), and at 1C/1C rate for 100 cycles (**B**).

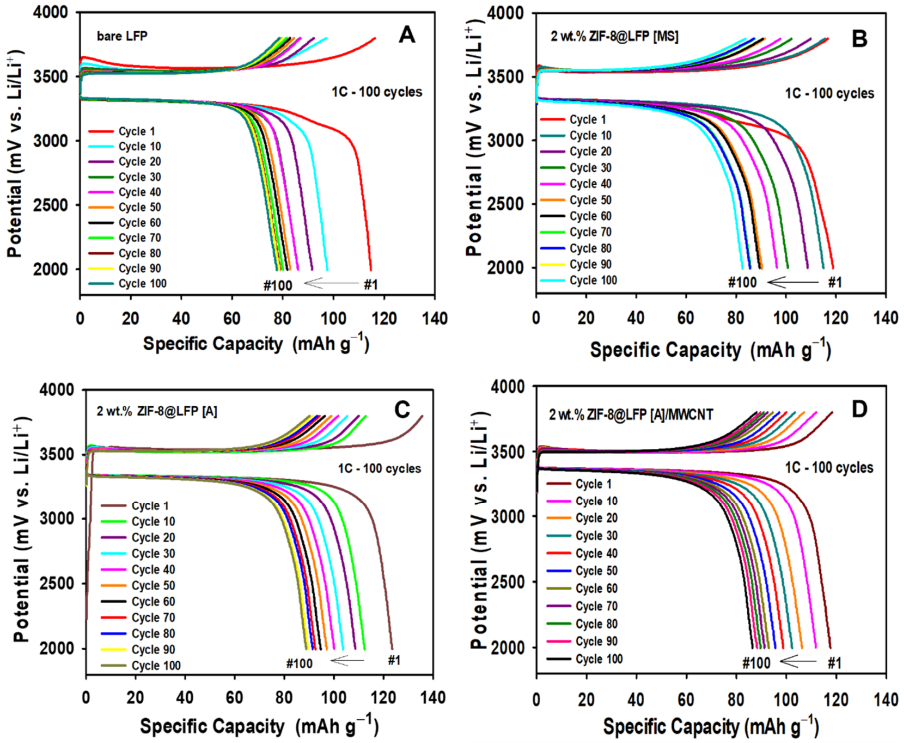

Figure 7. Charge–discharge curves of (**A**) bare LFP, (**B**) 2 wt.% ZIF-8@LFP [MS], (**C**) 2 wt.% ZIF-8@LFP [A], and (**D**) 2 wt.% ZIF-8@LFP [A]/MWCNT electrodes at 1C/1C rate for 100 cycles.

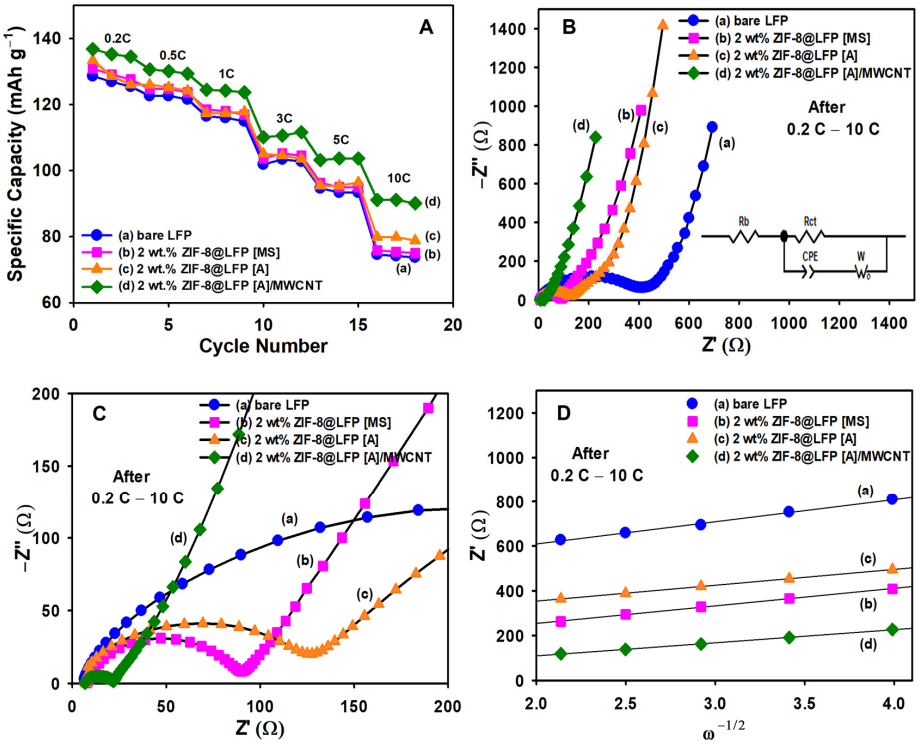

Figure 8. (**A**) High-rate profiles of the (a) bare LFP, (b) 2 wt.% ZIF-8@LFP [MS], (c) 2 wt.% ZIF-8@LFP [A], and (d) 2 wt.% ZIF-8@LFP [A]/MWCNT electrodes at various current rates of 0.2C, 0.5C, 1C, 3C, 5C, and 10C. (**B**) Nyquist plots of the (a) bare LFP, (b) 2 wt.% ZIF-8@LFP [MS], (c) 2 wt.% ZIF-8@LFP [A], and (d) 2 wt.% ZIF-8@LFP [A]/MWCNT electrodes after high-rate (*ca.* 0.2C–10C). (**C**) The magnified view of Figure 4B. (**D**) The linear dependence of Z' versus $w^{-1/2}$ for after high rate (*ca.* 0.2C–10C) cycles.

Table 1. Comparison of the high-rate performances 2 wt.% ZIF-8@LFP [A]/MWCNT composite cathode with previous reports.

Composite Cathodes	High-Rate Capacity (mAh g^{-1})				References
	1C	3C	5C	10C	
LFP@C_{ZIF-8}	142	-	92	59	[24]
LFP@C_{ZIF-8}	115	-	40	12	[25]
LFP@C-LATP	140	-	129	115	[13]
LFP/MWCNT	106	86	78	65	[47]
LFP@C-LALZO	110	-	70	-	[49]
LFP@C-VC	135	110	98	-	[50]
2 wt.% ZIF-8@LFP [A]/MWCNT	125	110	103	91	This work

Abbreviations: LFP—$LiFePO_4$; C_{ZIF-8}—ZIF-8 derived carbon; LATP–$Li_{1.3}Al_{0.3}Ti_{1.7}(PO_4)_3$; MWCNT—Multiwalled carbon nanotubes; LALZO—Al-doped $Li_{7-3x}Al_xLa_3Zr_2O_{12}$; VC—Vitamin C.

An electrochemical impedance spectroscopy (EIS) was implemented to study the reaction kinetics and the interfacial electrochemical trends of the as-prepared LFP electrodes. Nyquist plots were observed before (Figure S13A,B) and after (Figure 8B,C) the completion of high-rate cycling (about 18 cycles) at 0.2C to 10C rates of the as-fabricated electrodes, such as the bare LFP (a), 2 wt.% ZIF-8@LFP [MS] (b), 2 wt.% ZIF-8@LFP [A] (c), and 2 wt.% ZIF-8@LFP [A]/MWCNT electrodes (d). From the Nyquist plots, the electrode impedances, including bulk resistance (R_b), charge transfer resistance (R_{ct}), and total resistance ($R_T = R_b + R_{ct}$), can be estimated from the high-frequency semicircle region. In contrast, the Li^+ ion diffusion coefficient ($D_{Li}{}^+$) values were obtained from the low-frequency linear region. All these Nyquist plots are fitted by using the equivalent circuit mentioned in the inset of Figure 8B, which contains the elements, including R_b, R_{ct}, constant phase element (CPE), and Warburg impedance (W) [51,52]. Table 2 shows that the R_T value of 2 wt.% ZIF-8@LFP [A]/MWCNT electrode markedly reduced to 21.89 W, while the bare LFP was *ca.* 407.77 W. After the 10C rate, the R_{ct} value of 2 wt.% ZIF-8@LFP [A]/MWCNT electrode falls to 15.09 W, rather than the bare LFP electrode of 401.21 W. This reveals the improved electronic conductivity of the LFP composite materials, which enables its sustainability in high-rate operation. On the other hand, the uniform ZIF-8 coating on the LFP microspheres composite further markedly improved the Li^+ ion transfer properties. The $D_{Li}{}^+$ values of all the as-prepared LFP electrodes were calculated by the below Equation (1) [7]:

$$D_{Li^+} = \frac{R^2T^2}{2A^2n^4F^4C^2\sigma^2} \quad (1)$$

where R is the gas constant (9.314 J mol^{-1} K^{-1}), T is the absolute temperature (298 K), A is the surface area of the electrode (1.33 cm^2), n is the number of electrons per molecule during the redox reaction (n = 1 for the redox reaction of Fe^{3+}/Fe^{2+}), F is the Faraday constant (96,500 C mol^{-1}), C is the concentration of lithium-ions (7.69 × 10^{-3} mol cm^{-3}), and σ is the Warburg impedance factor. The σ values can be obtained from the slope of the linear relation of Z_{re} versus $\omega^{-1/2}$, based on the following Equation (2) [30]:

$$Z_{re} = R_b + R_{ct} + \sigma\omega^{-1/2} \quad (2)$$

Based on the obtained σ values, the $D_{Li}{}^+$ values were calculated before and after the high-rate cycling operation of the electrodes. The results are clearly summarized in Table 2. The $D_{Li}{}^+$ values are significantly increased after the high-rate charging-discharging conditions; this is due to the activation of Li^+ ion conduction channels after a few cycles. Our results show that the improvement of $D_{Li}{}^+$ values in the electrodes are based on the following order: bare LFP < 2 wt.% ZIF-8@LFP [MS] < 2 wt.% ZIF-8@LFP [A] < 2 wt.% ZIF-8@LFP [A]/MWCNT electrodes. The lowest impedance and highest $D_{Li}{}^+$ values indicated the low voltage polarization and high lithium transfer effect on the ZIF-8- and MWCNT-

modified LFP composite cathodes, respectively, and enhanced the high-rate electrochemical performance of the lithium-ion batteries.

The above results concluded that adding MWCNT via the mechanical alloy process is more beneficial for increasing the electron conductivity properties of 2 wt.% ZIF-8@LFP cathode materials, due to the highly conductive one-dimensional (1D) nanostructure of MWCNT. In chemical techniques, the MWCNT can be floated in the solution, due to the high surface area and nanofiber structure. Meanwhile, the ZIF-8 can also be deposited on the MWCNT, instead of growing on LFP particles. Hence, there is a possibility of reducing the electron-conductive nature of the MWCNT, when it is functionalized by ZIF-8 (poor electron conductor). Therefore, we have introduced MWCNT in a post-synthesis method. The mechanical alloy method helps microstructure of cathode materials to be well-attached with carbon nanostructured materials, due to the effective and fast milling of multicomponent.

Table 2. Summary of the impedance parameters of the electrodes before and after high-rate performances.

Parameters / Sample	R_b (Ω)		R_{ct} (Ω)		R_T (Ω) ($R_T = R_b + R_{ct}$)		D_{Li}^+ ($cm^2\ s^{-1}$)	
	Before	**After**	**Before**	**After**	**Before**	**After**	**Before**	**After**
Bare LFP	4.18	6.56	426.49	401.21	430.67	407.77	2.22×10^{-14}	3.40×10^{-14}
2 wt.% ZIF-8@LFP [MS]	6.51	7.69	181.10	82.38	205.86	90.07	6.92×10^{-15}	5.51×10^{-14}
2 wt.% ZIF-8@LFP [A]	4.10	6.98	274.10	120.65	278.20	127.63	1.72×10^{-14}	6.73×10^{-14}
2 wt.% ZIF-8@LFP [A]/MWCNT	3.85	6.82	193.00	15.09	196.85	21.89	8.41×10^{-15}	9.85×10^{-14}

In addition, the 1D fibrous structure MWCNT can deliver high electron conduction for long distances, rather than the zero-dimensional (0D) and two-dimensional (2D) carbon materials. Hence, the cathode materials are electronically connected by this 1D conductive carbon, rather than the 0D carbon. The high electron conductivity may also be affected while using the 2D conductive materials, due to the severe agglomeration or aggregation properties. Therefore, we prefer MWCNT for increasing the electron conductivity properties of the LFP cathode materials, thus improving the high-rate capacity in LIBs application. Furthermore, our proposed ZIF-8 coating method is a more facile, low-cost, and environmentally-friendly approach. The addition of MWCNT by mechanical alloy technology is also a less time-consuming and hazardous chemical-free process. So, the combination of both methods mentioned above is a suitable strategy for developing a composite cathode material with both electron/ions conducting properties for large-scale applications.

4. Conclusions

The ZIF-8 and MWCNT co-modified LFP composite material was prepared by using wet- and dry-coating methods. The optimum of 2 wt.% ZIF-8 coating exhibited superior electrochemical properties. The ZIF-8 nanoparticles uniformly deposited on LFP by an agitator method exhibit improved electrochemical Li^+ insertion/desertion kinetics, due to stabilizing the microstructure and increasing the Li^+ diffusion transport (ZIF8 immobilizing PF_6^- anions at the interface of electrode/electrolyte). Most importantly, the integration of the 1D conductive MWCNT on ZIF-8@LFP composite becomes an electron/ion transport frame network throughout the LFP cathode material. The successful incorporation of MWCNT in the 2 wt.% ZIF-8@LFP/MWCNT composite electrode manifests in the form of an elevated high-rate discharge capacity of 91.82 mAh g^{-1} at 10C rate. According to our proposed modification strategy, reduced voltage polarization and improved lithium-ion diffusion coefficient values have been observed. Therefore, our half-cell test results achieved higher Coulombic efficiency, high-rate capacities, and capacity retention. Thus, the as-synthesized 2 wt.% ZIF-8@LFP/MWCNT composite is an effective active cathode material for high-rate lithium-ion battery applications.

Supplementary Materials: The following supporting information can be downloaded at: https://www.mdpi.com/article/10.3390/batteries9030182/s1, Figure S1: SEM and XRD data of ZIF-8 nanoparticles; Table S1. Different formulation of ZIF-8 deposition on LFP materials; Figure S2: XRD patterns of the different (1, 2, 3, and 4 wt.%) ZIF-8@LFP composites, which were prepared by a magnetic stirring method; Figure S3: SEM images of the different (1, 2, 3, and 4 wt.%) ZIF-8@LFP composites, which were prepared by a magnetic stirring method; Figure S4. TEM images of the bare LFP and 2 wt.% ZIF-8@LFP [A]/MWCNT composite; Table S2: Comparative analysis of the intensity ratio (I_D/I_G) of the different LFP composite materials; Figure S5. XPS deconvolution spectra of O 1s, Fe 2p, P 2p and Li 1s peaks of the bare LFP and LFP composite (2% ZIF-8@LFP [A]/MWCNT); Figure S6: First charge–discharge cycles of the different (1, 2, 3, and 4 wt.%) ZIF-8@LFP composite electrodes, which were prepared by a magnetic stirring method; Table S3: Comparative electrochemical performance results for different ZIF-8@LFP formulations; Figure S7: Charge–discharge curves of the different electrodes at 0.1C/0.1C rate for 30 cycles; Figure S8. Average discharge voltage and voltage efficiency profile of the electrodes; Figure S9. SEM images for post-analysis of the electrodes; Figure S10. XRD pattens for post-analysis of the electrodes; Figure S11. EDX measurements for post-analysis of the electrodes; Figure S12: Charge–discharge curves of the different electrodes at various rate profiles of 0.2C–10C; Figure S13: Nyquist plot and Z′ versus $w^{-1/2}$ plot for before high rate (0.2C–10C) cycles.

Author Contributions: P.M.—conceptualization, methodology, investigation, and writing—original draft; J.-Y.S.—review and editing; Y.-J.J.L.—review and editing; T.-F.H.—review and editing; B.T.—investigation and validation; S.K.R.—review and editing; R.J.—review and editing; C.K.—conceptualization, validation, Software, writing—original draft, review, and editing and supervision; C.-C.Y.—supervision, resources, funding acquisition, review, and editing. All authors have read and agreed to the published version of the manuscript.

Funding: This research was supported by the Ministry of Science and Technology (MOST) of Taiwan from the University-Industry Cooperation Project (grant number MOST 108-3116-F-131-001-CC1) and MOST research project (grant number MOST 108-2221-E-131-022-MY3).

Informed Consent Statement: Not applicable.

Data Availability Statement: The data are available on reasonable request from the corresponding author.

Acknowledgments: We thank the Ministry of Science and Technology (MOST) of Taiwan for support through the University-Industry Cooperation Project (grant number MOST 108-3116-F-131-001-CC1) and MOST research project (grant number MOST 108-2221-E-131-022-MY3).

Conflicts of Interest: The authors declare no conflict of interest.

References

1. Manthiram, A. An Outlook on Lithium Ion Battery Technology. *ACS Cent. Sci.* **2017**, *3*, 1063–1069. [CrossRef]
2. Cao, Z.; Zhu, G.; Zhang, R.; Chen, S.; Sang, M.; Jia, J.; Yang, M.; Li, X.; Yang, S. Biological Phytic Acid Guided Formation of Monodisperse Large-Sized Carbon@$LiFePO_4$/Graphene Composite Microspheres for High-Performance Lithium-Ion Battery Cathodes. *Chem. Eng. J.* **2018**, *351*, 382–390. [CrossRef]
3. Wang, X.; Feng, Z.; Hou, X.; Liu, L.; He, M.; He, X.; Huang, J.; Wen, Z. Fluorine Doped Carbon Coating of $LiFePO_4$ as a Cathode Material for Lithium-Ion Batteries. *Chem. Eng. J.* **2020**, *379*, 122371. [CrossRef]
4. Cheng, Y.; Zhou, L.; Cai, X.; Cui, X.; Wu, S.; Pan, W.; Li, W. Effect of High-Energy Ball Milling Mixing Process on Electrical Performance and Synthesis Temperature of $LiFePO_4$/C Cathode Material. *Integr. Ferroelectr.* **2022**, *227*, 202–213. [CrossRef]
5. Huang, Y.; Liu, H.; Gong, L.; Hou, Y.; Li, Q. A Simple Route to Improve Rate Performance of $LiFePO_4$/Reduced Graphene Oxide Composite Cathode by Adding Mg^{2+} via Mechanical Mixing. *J. Power Sources* **2017**, *347*, 29–36. [CrossRef]
6. Erabhoina, H.; Thelakkat, M. Tuning of Composition and Morphology of $LiFePO_4$ Cathode for Applications in All Solid-State Lithium Metal Batteries. *Sci. Rep.* **2022**, *12*, 1–14. [CrossRef]
7. Zhou, Y.; Lu, J.; Deng, C.; Zhu, H.; Chen, G.Z.; Zhang, S.; Tian, X. Nitrogen-Doped Graphene Guided Formation of Monodisperse Microspheres of $LiFePO_4$ Nanoplates as the Positive Electrode Material of Lithium-Ion Batteries. *J. Mater. Chem. A* **2016**, *4*, 12065–12072. [CrossRef]
8. Wang, C.; Yuan, X.; Tan, H.; Jian, S.; Ma, Z.; Zhao, J.; Wang, X.; Chen, D.; Dong, Y. Three-Dimensional Carbon-Coated $LiFePO_4$ Cathode with Improved Li-Ion Battery Performance. *Coatings* **2021**, *11*, 1137. [CrossRef]
9. Yi, D.; Cui, X.; Li, N.; Zhang, L.; Yang, D. Enhancement of Electrochemical Performance of $LiFePO_4$@C by Ga Coating. *ACS Omega* **2020**, *5*, 9752–9758. [CrossRef] [PubMed]

10. Zhang, J.; Nie, N.; Liu, Y.; Wang, J.; Yu, F.; Gu, J.; Li, W. Boron and Nitrogen Codoped Carbon Layers of $LiFePO_4$ Improve the High-Rate Electrochemical Performance for Lithium Ion Batteries. *ACS Appl. Mater. Interfaces* **2015**, *7*, 20134–20143. [CrossRef]
11. Zhao, Q.F.; Yu, Y.H.; Ouyang, Q.S.; Hu, M.Y.; Wang, C.; Ge, J.H.; Zhang, S.Q.; Jiang, G.H. Surface Modification of $LiFePO_4$ by Coatings for Improving of Lithium-Ion Battery Properties. *Int. J. Electrochem. Sci.* **2022**, *17*, 221142. [CrossRef]
12. Yang, C.C.; Jiang, J.R.; Karuppiah, C.; Jang, J.H.; Wu, Z.H.; Jose, R.; Lue, S.J. LATP Ionic Conductor and In-Situ Graphene Hybrid-Layer Coating on $LiFePO_4$ Cathode Material at Different Temperatures. *J. Alloys Compd.* **2018**, *765*, 800–811. [CrossRef]
13. Nguyen, D.T.; Kim, J.; Lee, Y. A Hybrid Carbon–$Li_{1.3}Al_{0.3}Ti_{1.7}(PO_4)_3$ Conductive Coating for High Current Rate $LiFePO_4$ Cathode Material. *Chem. Eng. J.* **2023**, *7*, 141750. [CrossRef]
14. Mandal, S.; Natarajan, S.; Mani, P.; Pankajakshan, A. Post-Synthetic Modification of Metal–Organic Frameworks Toward Applications. *Adv. Funct. Mater.* **2021**, *31*, 1–22. [CrossRef]
15. Wang, Y.; Chen, B.; Zhang, Y.; Fu, L.; Zhu, Y.; Zhang, L.; Wu, Y. ZIF-8@MWCNT-Derived Carbon Composite as Electrode of High Performance for Supercapacitor. *Electrochim. Acta* **2016**, *213*, 260–269. [CrossRef]
16. Jafari, N.; Zeinali, S. Highly Rapid and Sensitive Formaldehyde Detection at Room Temperature Using a ZIF-8/MWCNT Nanocomposite. *ACS Omega* **2020**, *5*, 4395–4402. [CrossRef] [PubMed]
17. Xu, Q.; Jiang, H.; Li, Y.; Liang, D.; Hu, Y.; Li, C. In-Situ Enriching Active Sites on Co-Doped Fe-Co_4N@N-C Nanosheet Array as Air Cathode for Flexible Rechargeable Zn-Air Batteries. *Appl. Catal. B Environ.* **2019**, *256*, 117893. [CrossRef]
18. Liu, M.; Xiao, X.; Zhao, S.; Saremi-Yarahmadi, S.; Chen, M.; Zheng, J.; Li, S.; Chen, L. ZIF-67 Derived Co@CNTs Nanoparticles: Remarkably Improved Hydrogen Storage Properties of MgH_2 and Synergetic Catalysis Mechanism. *Int. J. Hydrogen Energy* **2019**, *44*, 1059–1069. [CrossRef]
19. Ashtiani, S.; Khoshnamvand, M.; Shaliutina-Kolešová, A.; Bouša, D.; Sofer, Z.; Friess, K. $Co_{0.5}Ni_{0.5}FeCrO_4$ Spinel Nanoparticles Decorated with UiO-66-Based Metal-Organic Frameworks Grafted onto GO and O-SWCNT for Gas Adsorption and Water Purification. *Chemosphere* **2020**, *255*, 126966. [CrossRef]
20. Hsu, L.F.; Venkatesh, K.; Karuppiah, C.; Ramaraj, S.K.; Yang, C.C. Incorporation of ZIF-67 Derived Co-N/C Core-Shell Nanoparticles on Functionalized MWCNT as a Highly Efficient Electrocatalyst for Nonenzymatic H_2O_2 Sensor. *Colloids Surfaces A Physicochem. Eng. Asp.* **2022**, *654*, 130133. [CrossRef]
21. Hira, S.A.; Park, K.H. Nitrogen-Doped Zeolitic Imidazolate Framework and Particle-Reduced Graphene Oxide Composites as Electrochemical Sensors and Battery-Type Supercapacitors. *ACS Appl. Nano Mater.* **2021**, *4*, 7870–7878. [CrossRef]
22. Tan, P.C.; Ooi, B.S.; Ahmad, A.L.; Low, S.C. Size Control and Stability Study of Zeolitic Imidazolate Framework-8 to Prepare Mixed Matrix Membrane. *J. Phys. Sci.* **2017**, *28*, 215–226. [CrossRef]
23. Li, B.; Li, G.; Zhang, D.; Fan, J.; Chen, D.; Liu, X.; Feng, T.; Li, L. Zeolitic Imidazolate Framework-8 Modified $LiNi_1/3Co_1/3Mn1/3O_2$: A Durable Cathode Showing Excellent Electrochemical Performances in Li-Ion Batteries. *Electrochim. Acta* **2020**, *336*, 135724. [CrossRef]
24. Xu, X.L.; Hao, Z.D.; Wang, H.; Liu, J.B.; Yan, H. Mesoporous Carbon Derived from ZIF-8 for Improving Electrochemical Performances of Commercial $LiFePO_4$. *Mater. Lett.* **2017**, *197*, 209–212. [CrossRef]
25. Xu, X.L.; Qi, C.Y.; Hao, Z.D.; Wang, H.; Jiu, J.T.; Liu, J.B.; Yan, H.; Suganuma, K. The Surface Coating of Commercial $LiFePO_4$ by Utilizing ZIF-8 for High Electrochemical Performance Lithium Ion Battery. *Nano-Micro Lett.* **2018**, *10*, 1–9. [CrossRef]
26. Zhou, X.; Wang, F.; Zhu, Y.; Liu, Z. Graphene Modified $LiFePO_4$ Cathode Materials for High Power Lithium Ion Batteries. *J. Mater. Chem.* **2011**, *21*, 3353–3358. [CrossRef]
27. Zhan, T.T.; Jiang, W.F.; Li, C.; Luo, X.D.; Lin, G.; Li, Y.W.; Xiao, S.H. High Performed Composites of $LiFePO_4$/3DG/C Based on $FePO_4$ by Hydrothermal Method. *Electrochim. Acta* **2017**, *246*, 322–328. [CrossRef]
28. Tsai, Y.D.; Shih, J.Y.; Li, Y.J.J.; Hung, T.F.; Hsu, L.F.; Ramaraj, S.K.; Jose, R.; Karuppiah, C.; Yang, C.C. Effect of Single-Walled Carbon Nanotube Sub-Carbon Additives and Graphene Oxide Coating for Enhancing the 5 V $LiNi_{0.5}Mn_{1.5}O_4$Cathode Material Performance in Lithium-Ion Batteries. *ACS Sustain. Chem. Eng.* **2022**, *10*, 16709–16724. [CrossRef]
29. Lei, X.; Zhang, H.; Chen, Y.; Wang, W.; Ye, Y.; Zheng, C.; Deng, P.; Shi, Z. A Three-Dimensional $LiFePO_4$/Carbon Nanotubes/Graphene Composite as a Cathode Material for Lithium-Ion Batteries with Superior High-Rate Performance. *J. Alloys Compd.* **2015**, *626*, 280–286. [CrossRef]
30. He, L.; Zha, W.; Chen, D. Fabrication and Electrochemical Properties of 3D Nano-Network $LiFePO_4$@multiwalled Carbon Nanotube Composite Using Risedronic Acid as the Phosphorus Source. *Prog. Nat. Sci. Mater. Int.* **2019**, *29*, 156–162. [CrossRef]
31. Zhang, J.; Huang, Z.; He, C.; Zhang, J.; Mei, P.; Han, X.; Wang, X.; Yang, Y. Binary Carbon-Based Additives in LiFePO4 Cathode with Favorable Lithium Storage. *Nanotechnol. Rev.* **2020**, *9*, 934–944. [CrossRef]
32. Musuvadhi Babulal, L.; Wu, S.H.; Yang, C.C. Surface Modification of Ni-Rich $LiNi_{0.8}Co_{0.1}Mn_{0.1}O_2$ Cathode Materials via a Novel Mechanofusion Alloy Route. *Ceram. Int.* **2020**, *46*, 22606–22618. [CrossRef]
33. Karuppiah, C.; Thirumalraj, B.; Alagar, S.; Piraman, S.; Li, Y.J.J.; Yang, C.C. Solid-State Ball-Milling of Co_3o_4 Nano/Microspheres and Carbon Black Endorsed $Lamno_3$ Perovskite Catalyst for Bifunctional Oxygen Electrocatalysis. *Catalysts* **2021**, *11*, 76. [CrossRef]
34. Sharmila, V.; Parthibavarman, M. Lithium Manganese Phosphate Associated with MWCNT: Enhanced Positive Electrode for Lithium Hybrid Batteries. *J. Alloys Compd.* **2021**, *858*, 157715. [CrossRef]
35. Nguyen, T.N.P.; Karuppiah, C.; Chien, W.C.; Wu, S.H.; Jose, R.; Lue, S.J.; Yang, C.C. Mechanical Alloy Coating of LATP Decorated Porous Carbon on $LiFe_1/3Mn_1/3Co_1/3PO_4$/C Composite Cathode for High-Voltage Li-Ion Battery. *Electrochim. Acta* **2020**, *359*, 136980. [CrossRef]

36. Venna, S.R.; Carreon, M.A. Highly Permeable Zeolite Imidazolate Framework-8 Membranes for CO_2/CH_4 Separation. *J. Am. Chem. Soc.* **2010**, *132*, 76–78. [CrossRef] [PubMed]
37. Cai, Y.; Huang, D.; Ma, Z.; Wang, H.; Huang, Y.; Wu, X.; Li, Q. Construction of Highly Conductive Network for Improving Electrochemical Performance of Lithium Iron Phosphate. *Electrochim. Acta* **2019**, *305*, 563–570. [CrossRef]
38. Song, J.; Shao, G.; Ma, Z.; Wang, G.; Yang, J. Synthesis of Hierarchical Conductive C/$LiFePO_4$/Carbon Nanotubes Composite with Less Antisite Defects for High Power Lithium-Ion Batteries. *Electrochim. Acta* **2015**, *178*, 504–510. [CrossRef]
39. Shih, J.Y.; Lin, G.Y.; Li, Y.J.J.; Hung, T.F.; Jose, R.; Karuppiah, C.; Yang, C.C. Operando Investigation on the Fast Two-Phase Transition Kinetics of LiFePO4/C Composite Cathodes with Carbon Additives for Lithium-Ion Batteries. *Electrochim. Acta* **2022**, *419*, 140356. [CrossRef]
40. Yuan, Y.; Xu, X.; Xia, J.; Zhang, F.; Wang, Z.; Liu, Q. A Hybrid Material Composed of Reduced Graphene Oxide and Porous Carbon Prepared by Carbonization of a Zeolitic Imidazolate Framework (Type ZIF-8) for Voltammetric Determination of Chloramphenicol. *Microchim. Acta* **2019**, *186*, 1–8. [CrossRef] [PubMed]
41. Yang, S.; Wang, Y.; Li, H.; Zhan, Y.; Ding, X.; Wang, M.; Wang, X.; Xiao, L. Synthesis of Nano-ZIF-8@chitosan Microspheres and Its Rapid Removal of p-Hydroxybenzoic Acid from the Agro-Industry and Preservatives. *J. Porous Mater.* **2021**, *28*, 29–38. [CrossRef]
42. Ran, J.; Chen, H.; Bi, S.; Guo, Q.; Deng, Z.; Cai, G.; Cheng, D.; Tang, X.; Wang, X. One-Step in-Situ Growth of Zeolitic Imidazole Frameworks-8 on Cotton Fabrics for Photocatalysis and Antimicrobial Activity. *Cellulose* **2020**, *27*, 10447–10459. [CrossRef]
43. Chiang, Y.C.; Chin, W.T. Preparation of Zeolitic Imidazolate Framework-8-Based Nanofiber Composites for Carbon Dioxide Adsorption. *Nanomaterials* **2022**, *12*, 1492. [CrossRef] [PubMed]
44. Pan, D.; Wang, L.; Li, Z.; Geng, B.; Zhang, C.; Zhan, J.; Yin, L.; Wang, L. Synthesis of Graphene Quantum Dot/Metal-Organic Framework Nanocomposites as Yellow Phosphors for White Light-Emitting Diodes. *New J. Chem.* **2018**, *42*, 5083–5089. [CrossRef]
45. Feng, S.; Jia, X.; Yang, J.; Li, Y.; Wang, S.; Song, H. One-Pot Synthesis of Core–Shell ZIF-8@ZnO Porous Nanospheres with Improved Ethanol Gas Sensing. *J. Mater. Sci. Mater. Electron.* **2020**, *31*, 22534–22545. [CrossRef]
46. Wu, S.; Zheng, H.; Wang, X.; Zhang, N.; Cheng, W.; Fu, B.; Chen, H.; Liu, H.; Duan, H. High-Capacity, Low-Tortuosity $LiFePO_4$-Based Composite Cathode Enabled by Self-Supporting Structure Combined with Laser Drilling Technology. *Chem. Eng. J.* **2022**, *430*, 132810. [CrossRef]
47. Kanagaraj, A.B.; Chaturvedi, P.; An, B.H.; AlDahmani, S.; Fadaq, H.; Choi, D.S. Electrochemical Performance of Freestanding $LiFePO_4$/MWCNT Composite Electrodes and Its Ex Situ Studies. *Ionics* **2020**, *26*, 115–125. [CrossRef]
48. Wu, F.; Kim, G.T.; Kuenzel, M.; Zhang, H.; Asenbauer, J.; Geiger, D.; Kaiser, U.; Passerini, S. Elucidating the Effect of Iron Doping on the Electrochemical Performance of Cobalt-Free Lithium-Rich Layered Cathode Materials. *Adv. Energy Mater.* **2019**, *9*, 1902445. [CrossRef]
49. Bai, Y.X.; Zhang, J.; Yang, Y.B.; Yang, R.; Yan, Y.L.; Wang, J. Enhance Electrochemical Performance of $LiFePO_4$ Cathode Material by Al-Doped $Li_7La_3Zr_2O_{12}$ and Carbon Co-Coating Surface Modification. *J. Alloys Compd.* **2020**, *843*, 154915. [CrossRef]
50. Lan, J.; Hou, H.; Huang, B.; Li, H.; Li, J. The Positive Role of Vitamin C in Spindle-like $LiFePO_4$/C Cathode Derived from Two Wastes. *Ionics* **2022**, *28*, 1583–1593. [CrossRef]
51. Rabiei Baboukani, A.; Khakpour, I.; Adelowo, E.; Drozd, V.; Shang, W.; Wang, C. High-Performance Red Phosphorus-Sulfurized Polyacrylonitrile Composite by Electrostatic Spray Deposition for Lithium-Ion Batteries. *Electrochim. Acta* **2020**, *345*, 136227. [CrossRef]
52. Allagui, A.; Baboukani, A.R.; Elwakil, A.S.; Wang, C. Electrochemical Stability Analysis of Red Phosphorus-Based Anode for Lithium-Ion Batteries. *Electrochim. Acta* **2021**, *395*, 139149. [CrossRef]